

Numerical Studies of Electromagnetic Flux-compression in θ -pinch Geometry

Contents

1. Introduction	44
2. Numerical model	44
2.1. Development of numerical modelling techniques at Loughborough	44
2.2. Filamentary modelling applied to θ -pinch electromagnetic flux-compression	45
2.3. Model equations	45
2.4. Numerical solution	50
3. Analysis of results from numerical experimentation	50
4. Experimental and theoretical comparison	53
5. Conclusions	55
Appendix: Electromagnetic force acting on a filament	56

Abstract

The paper presents a 2D numerical code, based on filamentary modelling techniques, that has been developed for simulation of the electromagnetic flux-compression process in θ -pinch geometry. Data obtained are compared with measured results from a recent experimental programme. It is shown that use of the code has highlighted various new and important aspects of the electromagnetic implosion technique.

1. Introduction

A recent paper [1] describes ongoing experimental work at Loughborough University into the development of highly efficient electromagnetic flux-compression for various applications. The considerable volume of experimentation required was minimised by the development of an accurate two-dimensional (2D) code, to enable the complete electromagnetic flux compression process to be accurately modelled. The present paper describes the code in detail, and verifies its accuracy by comparisons between theoretical and experimental results. Results are also presented from a large number of *numerical* experiments, to demonstrate the significance on the flux-compression process of the different parameters that are involved.

2. Numerical model

2.1. Development of numerical modelling techniques at Loughborough

Despite the geometric simplicity evident in the arrangement of figure 1, which is broken only by the feed to the single-turn coil, previous simulation attempts have failed to provide accurate predictions of the peak magnetic field. The first attempts, despite either drastic analytical approximations [2] or a grossly simplified approach [3], were nevertheless helpful in providing an understanding of basic features of the flux compression, although their implementation at Loughborough gave very disappointing results. The

first serious electromagnetic flux compression model proposed [4] was used successfully in the analysis of single-turn launchers [5], but it is unsuitable for the present application because of its lack of an adequate description of the magnetic diffusion through the liner wall. Attempts to improve the model by regarding the liner as consisting of a large number of cylindrical shells, in each of which different but uniformly distributed currents can flow, accounted for magnetic diffusion, but still gave poor results, even in the absence of an initial magnetic field.

It became clear that an accurate model must include a precise 2D representation of the liner current distribution, which can conveniently be based on the well-proven Loughborough filamentary technique [6]. However, in addition to determining the redistribution of this current during an implosion the model must also account accurately for the 2D liner and driving coil dynamics (a simplified 1D approach of the liner dynamics is presented in [7] and a model including the 1D driving coil dynamics is reported in [8]).

It also soon became clear that *the previously used magnetic pressure calculations [7] must be improved, as they include only part of the Maxwell stress* (see Appendix 1). This is perhaps one of the reasons why previous filamentary simulation attempts have failed to provide sufficiently accurate predictions of the peak magnetic field: the differences between the predicted and the measured peak field were 87 % in [7] and over 70 % in [8]. When the magnetic pressure corrections are implemented in a 2D dynamic filamentary model, very accurate overall predictions are indeed obtained in the absence of an initial magnetic field. Unfortunately, to obtain accurate results when this field is present requires a detailed definition of the initial field coil system, *neglected in all previously published filamentary models*, leading to a vastly greater number of filaments and a substantial increase in the computing time.

2.2. Filamentary modelling applied to θ -pinch electromagnetic flux-compression

As the current paths are assumed to be known in all the conducting elements of the system of figure 1, each of these can be divided into a large number of filamentary conductors. The filamentary cross sections are sufficiently small for a uniform current distribution to be assumed, and the filamentary resistances calculated simply as DC values. Due to the cylindrical symmetry evident in figure 1, all filamentary self-inductances and the associated inter-filamentary mutual inductances can be calculated using only two familiar formulae [9]. Straightforward circuit considerations then enable all the filamentary currents to be found and a complete mapping of the magnetic (and electric field, if required)

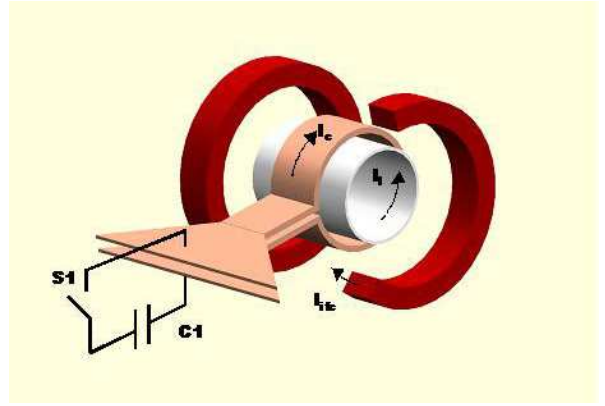


Fig. 1. Electromagnetic flux-compression arrangement with initial field injected cumulatively. Direction of liner current corresponds to first phase of compression. For simplicity initial field coil shields are omitted.

distributions to be obtained. The electromagnetic force distribution within the conductors can then be determined, and used to obtain the dynamics of the conductors for each time step. During integration of the equations of motion the conductors are assumed to be homogeneous and *incompressible*, and only after their new shapes and positions have been found can a new time step begin, with a corresponding new set of filamentary currents being defined. Conservation of the total system energy is used as a calculation check, and with sufficiently small time steps (normally between 1 ns and 5 ns) the variation was always much less than 1 %.

The model developed is not completely 2D since, although two independent space variables (radial and axial) are used, *axial movement is neglected* (and also any break in the cylindrical geometry). Axial dynamics are a very important issue as they influence the shape of the liner, particularly towards the end of implosion, precisely when the highest fields are generated. However, inclusion of a full 2D liner dynamics is beyond the reach of filamentary modelling and can only be properly taken into account by much more complex MHD or FEA (Finite Element Analysis) techniques. Efforts are being made at Loughborough to use the second technique and preliminary results will soon be published elsewhere.

In the present model the liner and the driving coil are considered as moving elements, and any movement of the other system elements relative to the initial field system is neglected. Although this assumption was confirmed as valid for the experimental situation at Loughborough, it would need to be re-examined for any other system investigated.

2.3. Model equations

The model must take into account the eight separate elements: driving coil c , liner l , two cylindrical shields

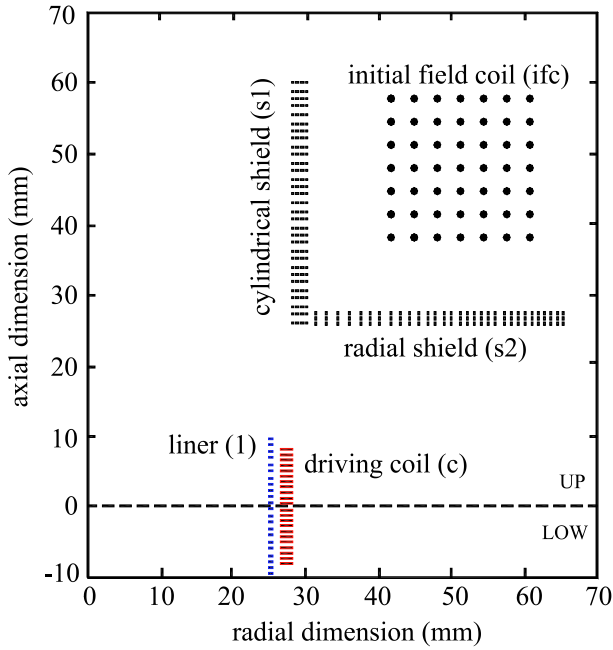


Fig. 2. Filamentary representation of elements.

s_1 , two radial shields s_2 , and two initial field coils ifc . Fortunately, all of these can be modelled by a collection of circular filaments with centres located as in figure 2. Consideration of their symmetry then enables the regions under investigation to be divided into an upper part UP and a lower part LOW, a technique pioneered in [10]. Furthermore, it is also convenient to regard the cylindrical shields as the upper and lower parts of the same component, as it is for the radial shields and the initial field coils. These simplifications mean that only the filamentary currents in the upper part need to be calculated.

Each part (UP or LOW) can be represented by a filamentary matrix having n columns and m rows, with row i corresponding to the same fixed axial distance when measured from the central plane of the region under investigation. The initial dimensions are selected so that all the filaments have the same mass. With radial dynamics considered for only the driving coil and the liner, and the materials regarded as incompressible, both the volume of all the filaments of every element and their axial position remain unchanged throughout an implosion. Under these restrictions, with the first filament having $i = 0$, the axial δz and radial δr dimensions and the axial z and radial r positions of the filaments are given by

$$\delta z = \frac{Z}{2m}, \quad (1)$$

$$\delta r(i, R_1) = \sqrt{\frac{S}{n\pi}(\text{mod}(i, n) + 1)R_1^2} - \sqrt{\frac{S}{n\pi}\text{mod}(i, n) + R_1^2}, \quad (2)$$

$$z(i) = \left[\text{floor} \left(\frac{i}{n} \right) + \frac{1}{2} \right] \frac{Z}{2m}, \quad (3)$$

$$r(i, R_1) = \sqrt{\frac{S}{n\pi}(\text{mod}(i, n) + 1) + R_1^2}, \quad (4)$$

where Z is the axial dimension of the element, $S = \pi [(R_1^0 + \text{thick})^2 - (R_1^0)^2]$ is the constant cross section and $\text{mod}(i, n)$ and $\text{floor}(x)$ are subroutines returning the remainder of i when divided by n and the greatest integer $\leq x$ respectively.

In the cases of the driving coil and liner, each row is allowed to move independently and R_1 is therefore a time dependent vector representing the inner radius of the rows, with the specific row number for the filament i being determined by $\text{floor}(i/n)$. R_1^0 is the initial value of R_1 and $\text{thick} = R_2^0 - R_1^0$ is the initial thickness where R_2 is the time dependent outer radius. Note that only the row inner radius R_1 determines the radial position and dimension of each filament.

In the same way, using the incompressibility properties, the radial velocity of each filament is determined from the relation

$$\nu(i, R_1, V_1) = \frac{V_1 R_1}{r(i, R_1)}, \quad (5)$$

where the time dependent vector V_1 represents the inner radial velocity of rows. The outer radius and velocity are given respectively by $R_2 = \sqrt{S/\pi + R_1^2}$ and $V_2 = V_1 R_1 / R_2$.

To calculate the filamentary currents, the time-dependent vector $DIDT$ containing the rates of change of filamentary currents is obtained from the solution of the system algebraic core matrix equation, using the LU decomposition method for matrix inversion [11]

$$DIDT = Matrix^{-1}Voltage \quad (6)$$

The time-dependent symmetrical square $Matrix$ can be written as

$$Matrix = \begin{pmatrix} l & l/c & l/s_1 & l/s_2 & l/ifc \\ & c & c/s_1 & c/s_2 & c/ifc \\ & & s_1 & s_1/s_2 & s_1/ifc \\ & & & s_2 & s_2/ifc \\ & & & & ifc \end{pmatrix}$$

where each matrix region represents a single element (l, c, s_1, etc) that contains, as non-diagonal terms, mutual inductances between pairs of different filaments of that element and on the main diagonal self-inductances. The only exception is the diagonal terms of region c that contain, in addition to the self-inductance, twice the total inductance of the main bank. Those regions that represent the interaction between various elements ($l/c, s_1/s_2, etc$) contain only mutual inductances.

It is very important to note that, since only one half of the filamentary currents are being calculated,

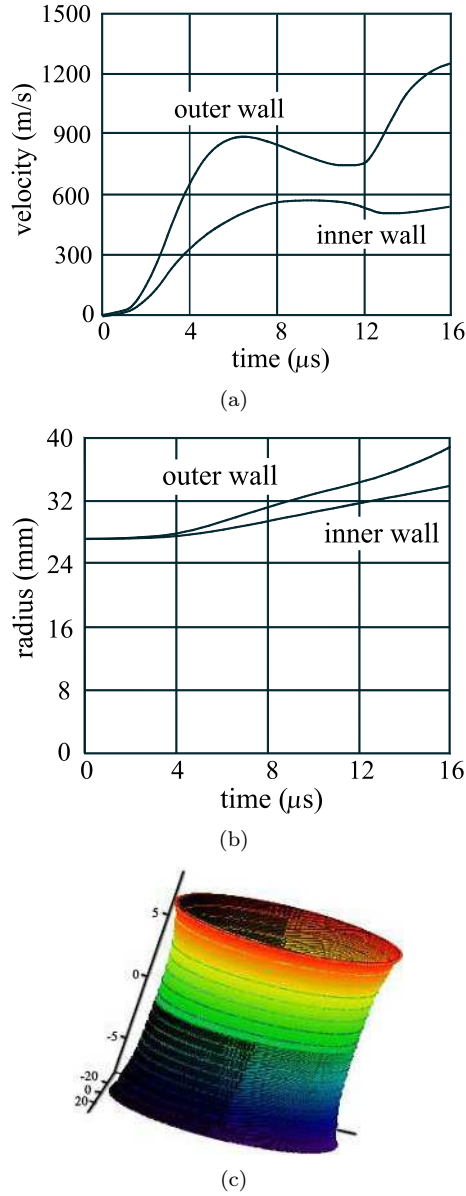


Fig. 3. Driving coil dynamics: a) – inner and outer wall velocities at centre; terminal velocity about 2 km/s; b) – inner and outer central wall radius; c) – driving coil shape close to instant of peak field (12 μ s) (still from an AVI movie).

each non-diagonal component (i, j) of *Matrix* is in fact the sum of two mutual inductance terms, one representing the mutual inductance between a pair (i, j) of filaments situated in the UP region and the other the mutual inductance for the same pair (i, j) , but with one of the filaments situated in the LOW region.

The *ifc* region contains only one diagonal term, as only one current flows through the initial field coils. This term represents the total inductance of the initial field system, and is calculated simply as $Indifc = 2(Indonecoil + Mutcoils) + Indifcbank$. *Indonecoil* is the self-inductance of one coil, and is obtained

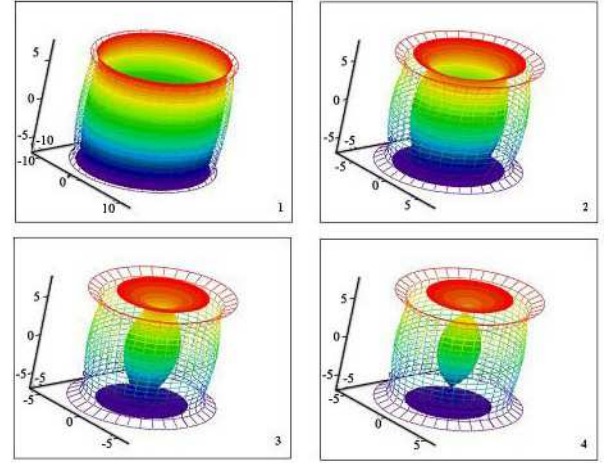


Fig. 4. S design liner [1] dynamics (stills from an AVI movie). Note complete collapse at both ends (frame 4) due to the axial dimension of the liner being shorter than that of the driving coil.

by summing all the self-inductances with twice the various mutual inductances between all the filaments representing the winding turns. *Mutcoils* represents the mutual inductance between two identical coils, and is again calculated as twice the sum of the mutual inductances between all possible pairs of filaments of the two coils. *Indifcbank* is the total inductance of the initial field bank including the transmission cables.

The mutual inductance terms in *Matrix* between any filament of any element and the *ifc* element are calculated as a sum of the mutual inductances between that filament and all the filaments of the *ifc* coil.

As an example some components of the time-dependent *Voltage* vector are

- for the liner currents I_{li}

$$\begin{aligned}
 Voltage_i = & - \left\{ Rl_i I_{li} \right. \\
 & + \sum_j (DMiUP_{i,j} + DMiLOW_{i,j}) I_{lj} \\
 & + \sum_j (DMlcUP_{i,j} + DMlcLOW_{i,j}) I_{cj} \\
 & + \sum_j (DMls_1UP_{i,j} + DMls_1LOW_{i,j}) I_{s1j} \\
 & + \sum_j (DMls_2UP_{i,j} + DMls_2LOW_{i,j}) I_{s2j} \\
 & \left. + (DMl_{ifc}UP_i + DMl_{ifc}LOW_i) I_{ifc} \right\}
 \end{aligned}$$

- for the driving coil currents I_{ci}

$$\begin{aligned}
 Voltage_i = & V_0 - \left\{ \frac{Q_1}{C_1} + 2Rbank \sum_j I_{cj} + Rc_i I_{ci} \right. \\
 & \left. + \sum_j (DMccUP_{i,j} + DMccLOW_{i,j}) I_{cj} \right\}
 \end{aligned}$$

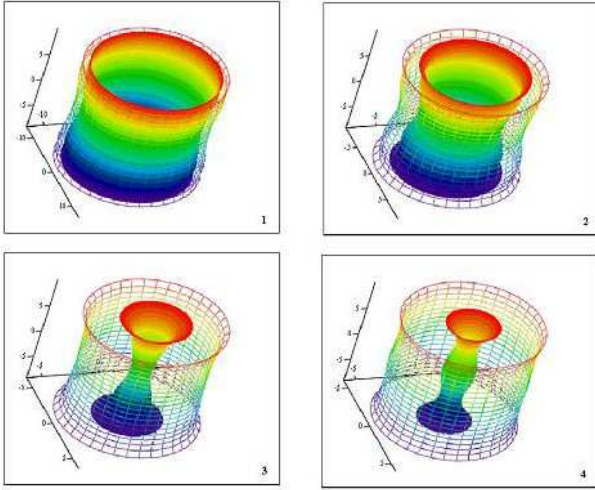


Fig. 5. M design liner [1] dynamics (stills from an AVI movie). Note turnaround phenomenon (frame 4) due to the axial dimension of the liner being longer than that of the driving coil.

$$\begin{aligned}
 & + \sum_j (DMclUP_{i,j} + DMclLOW_{i,j}) \\
 & + Il_j \sum_j (DMcs_1UP_{i,j} + DMcs_1LOW_{i,j}) Is_{1j} \\
 & + \sum_j (DMcs_2UP_{i,j} + DMcs_2LOW_{i,j}) Is_{2j} \\
 & + (DMc_{ifc}UP_i + DMc_{ifc}LOW_i) I_{ifc} \}. \quad (7)
 \end{aligned}$$

The other components are calculated in a similar way, with the j summations taken over all the upper (or lower) number of filaments of that element as appropriate.

In the equations above, V_0 , C_1 , R_{bank} and Q_1 are respectively the initial voltage and capacitance of the main capacitor bank, the total resistance (including transmission plates and switch) and the charge delivered to the main circuit. R_i represents a filamentary resistance calculated as a DC resistance.

The time rate-of-change of mutual inductance between various filaments is represented by terms containing DM. The first filament is *always* in the upper region but the second can be in either the upper or the lower region. As an example, $DMclLOW$ represents the time rate-of-change of mutual inductance between a driving coil filament (in the UP region) and a filament in the LOW region of the liner. Numerical calculation of these terms is based on the following formula, where, for convenience, R_1 and V_1 are discarded from terms such as $r(i, R_1)$ or $v(i, R_1, V_1)$

$$\left(\frac{dM}{dt} \right)_{i,j} = \frac{M(r(i), r(j), \Delta z_{i,j})}{2} \left(\frac{v(i)}{r(i)} + \frac{v(j)}{r(j)} \right)$$

$$- \frac{2 - k^2}{k(1 - k^2)} dk \Big) + \frac{\mu k^2 \sqrt{r(i)r(j)}}{2(1 - k^2)} K(k) dk.$$

Calculations of the mutual inductance between two filaments employs the complete elliptic integrals of the first $E(k)$ and second kind $K(k)$ [9]

$$\begin{aligned}
 M(r(i), r(j), \Delta z_{i,j}) &= \frac{2\mu\sqrt{r(i)r(j)}}{k} \\
 &\times \left[\left(1 - \frac{k^2}{2} \right) K(k) - E(k) \right] \quad (8)
 \end{aligned}$$

where the modulus of k is obtained from

$$k^2 = \frac{4r(i)r(j)}{(r(i) + r(j))^2 + \Delta z_{i,j}^2}$$

and

$$\begin{aligned}
 dk &= \frac{k}{2} \left[\frac{v(i)}{r(i)} + \frac{v(j)}{r(j)} \right. \\
 &\quad \left. - (\nu(i) + \nu(j)) \left(\frac{1}{r(i)} + \frac{1}{r(j)} \right) \frac{k^2}{2} \right].
 \end{aligned}$$

In deriving the dM/dt formula the following properties of E and K are also used [9]

$$\frac{dK}{dk} = \frac{E}{k(1 - k^2)} - \frac{K}{k} \quad \text{and} \quad \frac{dE}{dk} = \frac{E}{k} - \frac{K}{k}$$

$\Delta z_{i,j} = |z(i) - z(j)|$ when both filaments are situated in the UP region but if the second filament is in the LOW region $\Delta z_{i,j} = z(i) + z(j)$.

Because of the very many similar calculations during each program run, it is *vital* that extremely fast subroutines are implemented for calculating both the mutual inductances and the elliptic integrals. As the main program was written in MATHCAD, these were written in C++ [11] and implemented as dynamic linked library (DLL) functions.

Calculated results for the self-inductance of an infinitesimal filament diverge as the cross-section area reduces and the results are therefore unrealistic. The self-inductance of a filament with a finite square cross section, on the other hand, is realistic but cannot easily be accurately calculated. The next best approximation that can be adopted is a filament with circular cross-section, which works for single-turn coil simulation but still gave rise sometimes to numerical problems in the present case. The approximation used in the present paper is that of an infinitely thin ribbon with finite axial extension, which is closer to an infinitesimal filament, and hence gives larger (and less realistic) values. The formula is taken from [7] and avoids numerical problems otherwise arising from an incompatibility, sometimes causing values from mutual inductance calculations based on infinitely small filaments (equation (7)) to exceed the associated self inductances calculated for a finite cross-section ring [5].

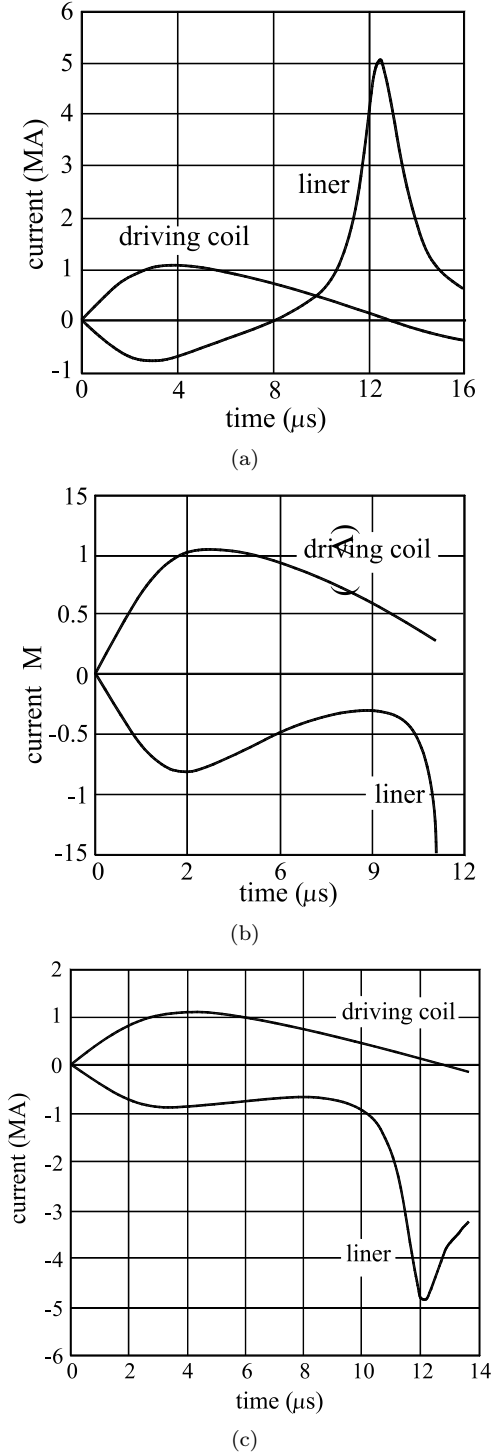


Fig. 6. Predicted system currents for numerical experiments with an aluminium M design liner and initial field: a) – 2.5 T cumulatively injected; kinetic/electrostatic efficiency 25 %, liner turns around before reaching the probe outer diameter; central peak field about 350 T; b) – 2.5 T differentially injected; calculations cease once liner makes contact with the probe, corresponding central field is only 50 T; c) – 5.8 T differentially injected; kinetic/electrostatic efficiency 47.8 %, liner turns around before reaching the probe outer diameter; central peak field about 430 T.

The solution for the system of differential equations sometimes tends to diverge. However, this divergence if it appears, is not caused by the inductances but by the fact that a pair of filamentary currents differ too much, which happens if the filament size chosen is too large (to reduce the filament number and thus to speed up the computation). If required, this unwanted effect can be artificially compensated by assuming a larger self-inductance.

When obtaining the filamentary temperature and its influence on the electrical conductivity σ , the time rate-of-change of the specific Joule deposited energy W is calculated for each filament, thus

$$\frac{dW_i}{dt} = \frac{I_i^2}{\delta r(i)^2 \delta z^2 \sigma(W_i)}. \quad (9)$$

The Los Alamos National Laboratory SESAME tabulated equations of state [12] were used to obtain the temperature from the specific energy for aluminium (the liner) and copper (the driving coil and initial field coils). As thermal effects are small, a very crude model [13] was adopted for the stainless steel of the shields. A relatively new theoretical model was used for the temperature variation of the electrical conductivity of the aluminium and copper [14], while for stainless steel a crude approximation [13] was again considered to be adequate. It should be mentioned that, due to the incompressibility hypothesis adopted throughout the analysis, no influence of pressure on either the equation of state or the electrical conductivity could be included.

The dynamic equations for the rows of both the driving coil and liner filaments are [7]

$$\frac{dV_1}{dt} = \frac{1}{R_1} \left[\frac{P}{\rho} + \frac{V_1^2 S}{2\pi R_2^2} - V_1^2 \right], \quad (10)$$

$$\frac{dR_1}{dt} = V_1, \quad (11)$$

where ρ is the mass density. The pressure P acting on a row is calculated as a sum of filamentary pressures, with each pressure calculated as the total radial force acting on a filament divided by its lateral surface area $\delta z \delta r$. Radial forces acting on a filament i are calculated using equation (A5), where B_{ext}^z is calculated as the resultant axial magnetic flux density produced by the other filaments with elementary contributions j given by [9]

$$B_j^z = \frac{\mu_0 I_j}{2\pi} \frac{1}{\sqrt{(r(i) + r(j))^2 + \Delta z_{i,j}^2}} \times \left[K(k) + \frac{r(i)^2 - r(j)^2 - \Delta z_{i,j}^2}{(r(i) - r(j))^2 + \Delta z_{i,j}^2} E(k) \right], \quad (12)$$

where the same simplifications as in equation (7) apply.

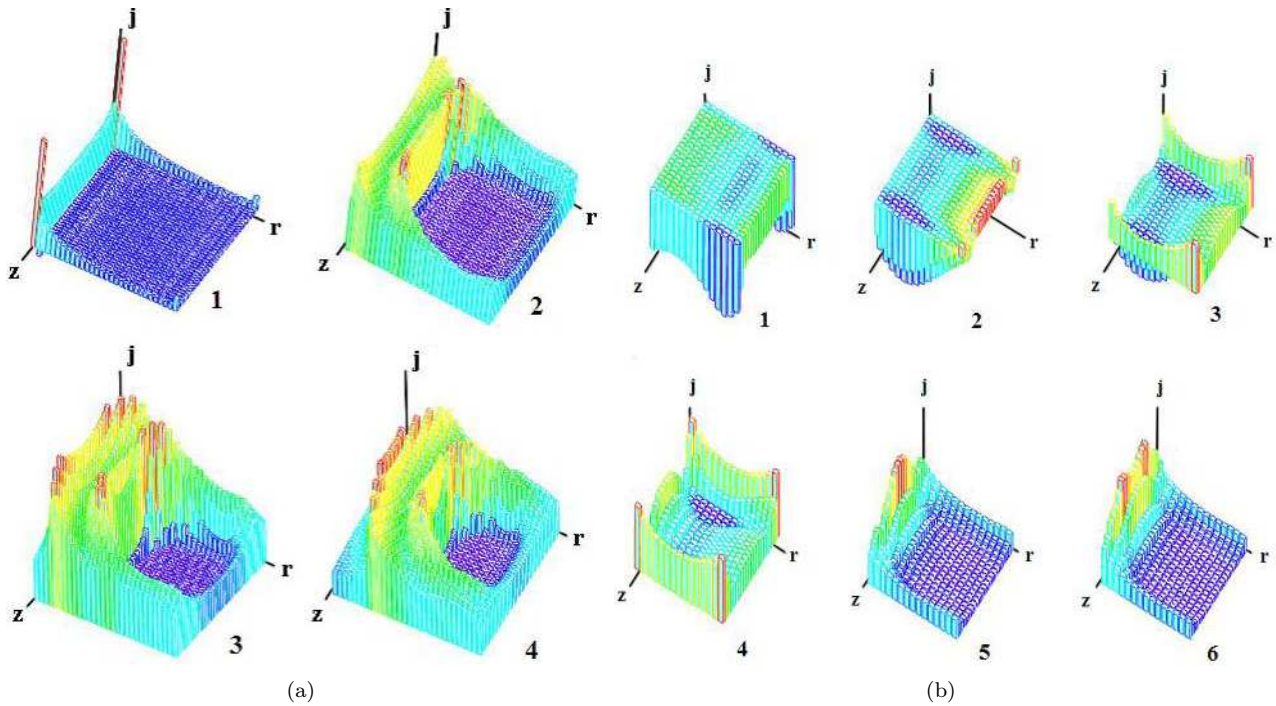


Fig. 7. Typical history of current density (j) distribution: a) in a single-turn coil during a fast bank discharge and b) in a liner design M during a fast electromagnetic flux compression. Only right-side cross section is shown in cylindrical coordinates r, z . Times are for (a) 1: 200 ns; 2: 400 ns; 3: 600 ns; 4: 900 ns and for (b) 1: 3 μ s, 2: 6 μ s, 3: 8 μ s, 4: 9 μ s, 5: 11.5 μ s and 6: 12 μ s.

2.4. Numerical solution

Use of a Runge-Kutta subroutine provides a very convenient technique for the numerical integration of the set of first-order differential equations (6),(8),(9) and (10). The usual number of filamentary currents calculated for each element are indicated in parentheses as $c(66), l(165), s_1(186), s_2(186)$, giving a system of 1407 differential equations to be solved, including those for the Joule energy deposited in the resistance of the main and initial field capacitor banks and in the safety fuses (sometimes) used in their circuits.

The time required for integration is however relatively long, almost one day when using a 2.4 GHz PC. For parametric studies, a *reduced model* neglecting details of the initial field coil and shields (but taking into account the initially injected magnetic field distribution) and having a reduced number of filaments in some of the elements is therefore used, which lowers the time of integration to about one hour.

Once the integration is complete, the magnetic field distribution at any time can be easily calculated as the total filamentary field, with each contribution obtained using equation (11). If required, the electric field distribution can also easily be obtained.

The above program can be straightforwardly used for simulating single-turn discharges, when only one element (the single-turn "driving" coil) is taken into

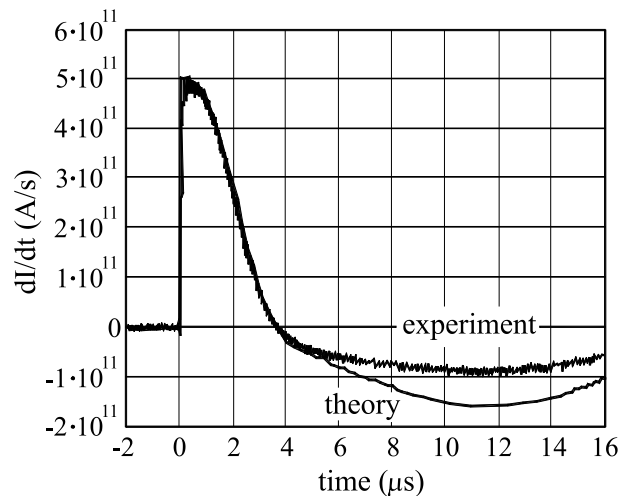


Fig. 8. Time rate-of-change of driving coil current: experimental signal and predicted variation.

account. The resulting program is extremely fast and efficient.

3. Analysis of results from numerical experimentation

The reduced computer model was used in an investigation of the multiparameter space of the

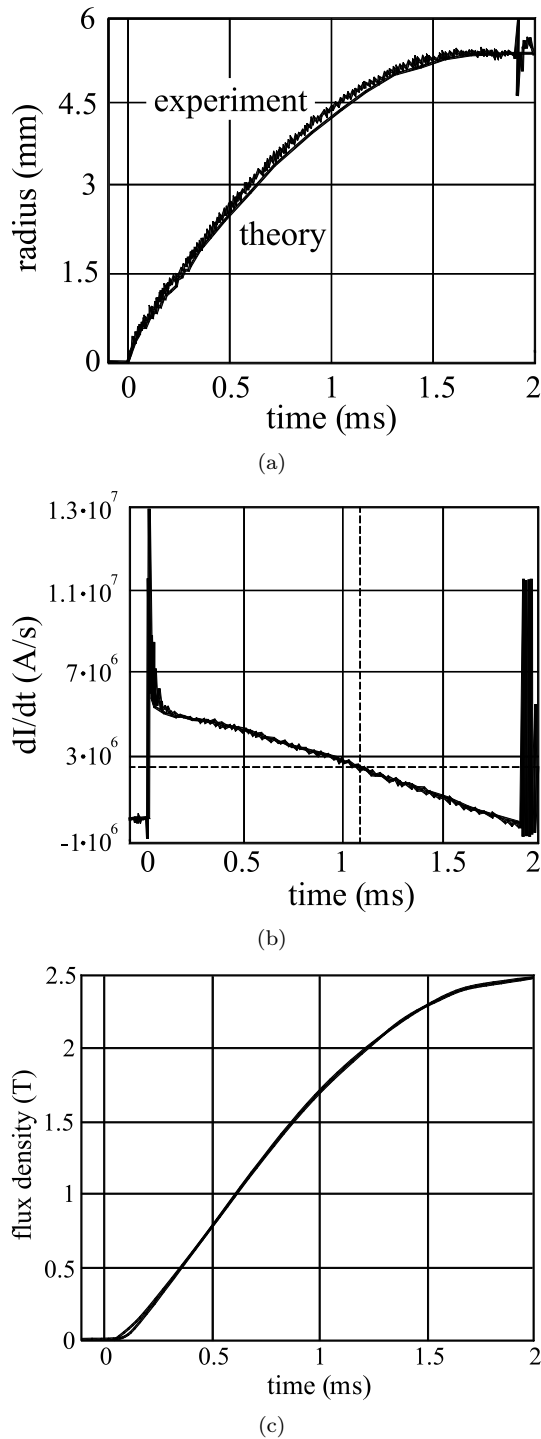


Fig. 9. Characteristics of initial field coil [1], measured and predicted. a) – current I_{ifc} (Rogowski); b) – dI_{ifc}/dt (transformer) and c) – central magnetic field Bifc (t) (integrated pick-up probe). (a) and (b) are for a flux compression experiment, (c) is for a preliminary initial field experiment (without implosion). Shape of signals at beginning of discharge shows diffusion of field through shields and liner. Disturbance after 1.9 ms is due to start-up of 100 kV Marx generator [1].

system, such as the effect of the axial and radial dimensions of the coil and the liner, different liner materials and initial temperatures, strength of the initial injected field, etc. The main result of this study was the three liner designs described below. A number of significant findings emerged when the overall system performance of these designs was analysed in detail using the full code, and the most important of these are summarised below. Although some of the findings have been reported elsewhere [7], most are undoubtedly new. All should however be regarded with caution, as the model does not account for important perturbing effects such as the unavoidable driving coil slit, liner 3D dynamics, elasto-plasticity of the materials and the generation of shock waves.

- (i) *The driving coil can be thin.* In most practical cases inertial forces are sufficient to preserve the initial coil shape during a *fast* implosion, as illustrated by figure 3. This is very valuable, since a thin coil will maintain a high coil/liner mutual inductance and limit the current redistribution due to diffusion and heating and so provide a high electrostatic to kinetic energy conversion efficiency.
- (ii) *The axial dimension of the liner should be longer than that of the driving coil.* If the liner is shorter than the driving coil, it is predicted [7] that the high temperature produced at the liner extremities may be sufficient to cause vapourisation. By using 2D dynamics for both liner and driving coil, the present code demonstrated however that the convex axial profiling appearing during an implosion partially compensated for this effect. However it also reduced the possibility of measuring the maximum magnetic field strength produced on the common axis, see figure 4, by either cutting the connections to an electromagnetic pick up probe or interrupting the light beam of a magneto-optic sensor. In practice the problem can be overcome by using a liner slightly longer than the coil, when, as figure 5 shows, a concave axial profile is developed.
- (iii) *Three interacting designs are possible for any particular power supply.* A *small* diameter coil/liner design (an S design) is best suited for obtaining the highest implosion velocities with a low level of instabilities. In principle a high velocity of the liner is advantageous, but to generate efficiently ultrahigh magnetic fields the liner has to be stopped by magnetic pressure and its kinetic energy transferred to the field. Calculations proved however that this will not happen at practical diameters, unless a relatively high initial field is injected. Since however the initial field strength is limited by the available power supply, a *medium* diameter coil/liner

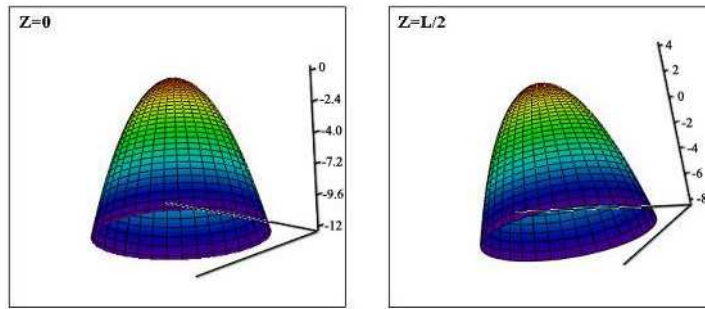


Fig. 10. Radial magnetic field distribution produced by initial field coils inside M design liner of length L (a) at a central section ($Z=0$) and (b) at an extremity ($z=L/2$). Values shown on the vertical axis are a percentage of the field at the liner centre. The base circle corresponds to the liner inner diameter.

design (an M design) will generate the strongest field obtainable from a given system for the given diameter of the magnetic probe. Very careful tuning of the initial field strength is needed, as relatively small changes can have a drastic negative effect (as shown by results with too high an initial magnetic field in [15]). The peak field is obtained when the 'turnaround' diameter of the liner is close to, but greater than, the probe diameter. In most applications however, an increased final diameter is required, and for any given power supply the (lower) maximum field that can be generated is obtained with a *high* diameter coil/liner design (an H design). Full details of the three designs appropriate for the Loughborough power supply are given elsewhere [1].

- (iv) *Either a cumulative or a differential initial field may be injected (i.e. either in the same direction as, or the opposite direction to, the field produced by the driving coil).* Figure 6(a) shows the system currents predicted for the particular M design with an initial field of 2.5 T injected cumulatively, as is the presently the norm. In this case the liner current reverses during the implosion, which causes the electromagnetic force to change in direction and the driving coil to attract the liner. Figure 6(b) shows that no similar reversal occurs when the same initial field is injected differentially. Although in principle this results in a saving in electromagnetic energy, the peak field is produced in too small a volume to be of any practical consequence, leading previous experimentalists to conclude that differentially injected fields are not useful. However, as now predicted for the M design, a differentially injected field *about twice that cumulatively injected* gives an increased peak field at the (unchanged) turnaround diameter, with the corresponding currents being presented in figure 6(c). When adopted, this new technique will also help in achieving

higher kinetic/electrostatic energy efficiency and perhaps even an improved quality of implosions, as the imploding force is maintained until the peak field is generated. Practical investigation of this technique unfortunately requires a higher energy capacitor bank than is presently available at Loughborough.

- (v) *The liner material plays a very important role in the efficiency of magnetic flux-compression.* As an example, use of (more expensive) copper liners instead of (easy to manufacture) aluminium liners can increase substantially the peak field. Calculations show that for a Loughborough M design arrangement, with an initial field of 2.5 T cumulatively injected, the predicted peak field for an aluminium liner with a final diameter exceeding 2.5 mm is around 350 T, while for a copper liner it is around 430 T. The difference is mainly a consequence of the better electrical conductivity of copper and not of mechanical and thermal effects. In both cases calculations show that only part of a thin inner layer of the liner is at the melting temperature.
- (vi) *In principle, electromagnetic flux compression is more effective than the single-turn technique in producing ultrahigh magnetic fields from a given high-current fast power source.* In a single-turn coil the initial current density is higher on the inner side of the coil, with peaks occurring at the axial extremities. As however the capacitor discharge progresses, the high temperature generated in these positions and the coil dynamics both speed-up relocation of the current distribution from the extremities towards the centre and from the inner surface towards the outer (figure 7a). In an imploding liner with an initial cumulatively injected field the initial current density is higher at the outer surface, with the temperature correspondingly greater. At some time during the implosion, most of the filamentary currents reverse in direction

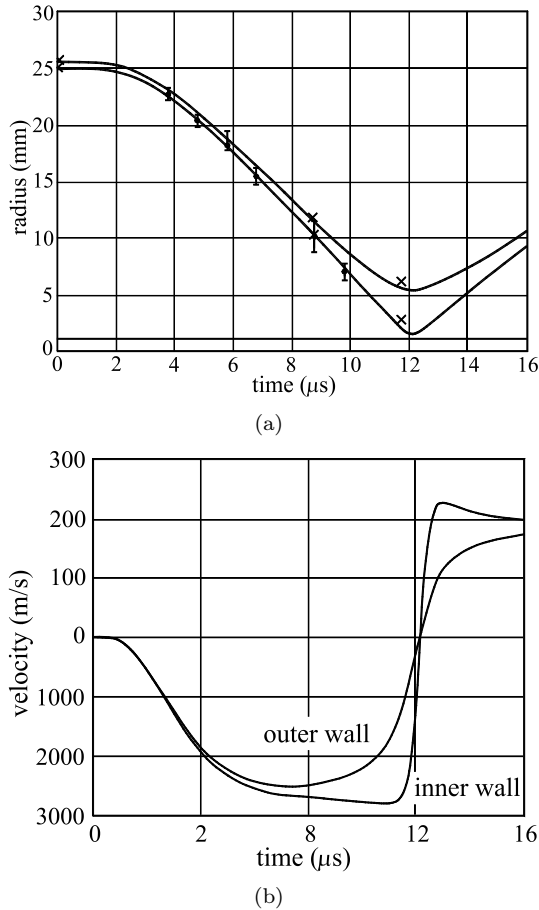


Fig. 11. a) – Liner wall dynamics (initial field present). Experimental points from photographs and 'Xs' from x-ray picture, provided by identical experiments. Position of the ceramic tube outer diameter, housing the magnetic probe, is also shown. b) – Predicted midpoint inner and outer wall velocities (initial field present).

(see figure 7b-4). The current distribution subsequently spreads *uniformly* (figure 7b-5 and 6) on the *cooler* inner surface, which certainly provides the best condition for producing an ultrahigh central magnetic field. The total current in the liner eventually reaches many MAs, much exceeding the maximum current that can be provided by most capacitor banks.

4. Experimental and theoretical comparison

Since space limitations preclude comparisons between experimental and theoretical data for all three liner designs, the considerations below refer only to the M design, both with and without any initial field. All experimental details correspond to the data

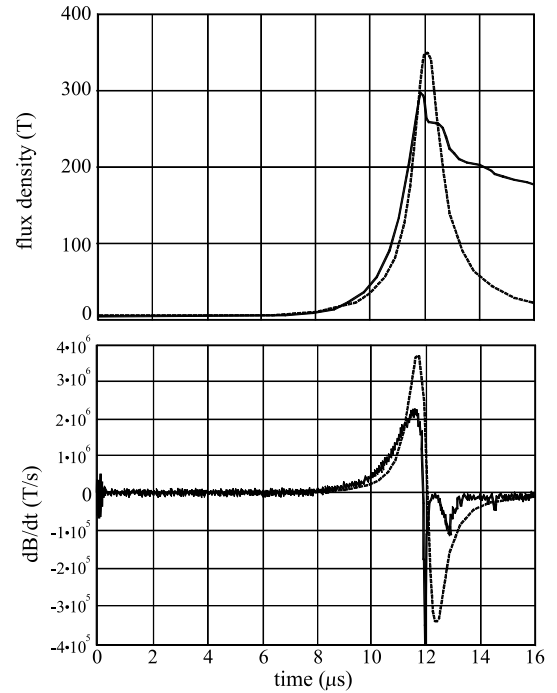


Fig. 12. Upper: time history of magnetic field (integrated dB/dt signal) from a M design liner implosion with initial field present, compared with theoretical predictions (dotted line). Lower: dB/dt signal compared with theoretical predictions (dotted line).

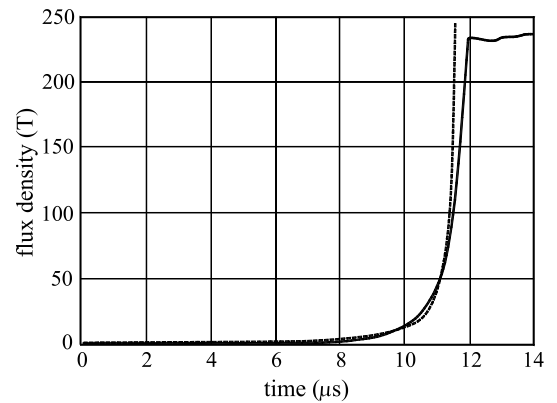


Fig. 13. Time history of magnetic field (integrated dB/dt signal) from a M design liner implosion without initial field, compared with theoretical predictions (dotted line).

presented elsewhere [1].

Figure 8 shows the time rate-of-change of current in the driving coil, and very good agreement clearly exists up to about $4 \mu s$. The discrepancies that appear beyond this time are attributed to the development of a plasma cloud around the driving coil [16], that introduces a progressively reducing electrical resistance in parallel with the driving coil.

Figure 9 shows the current in the initial field coil

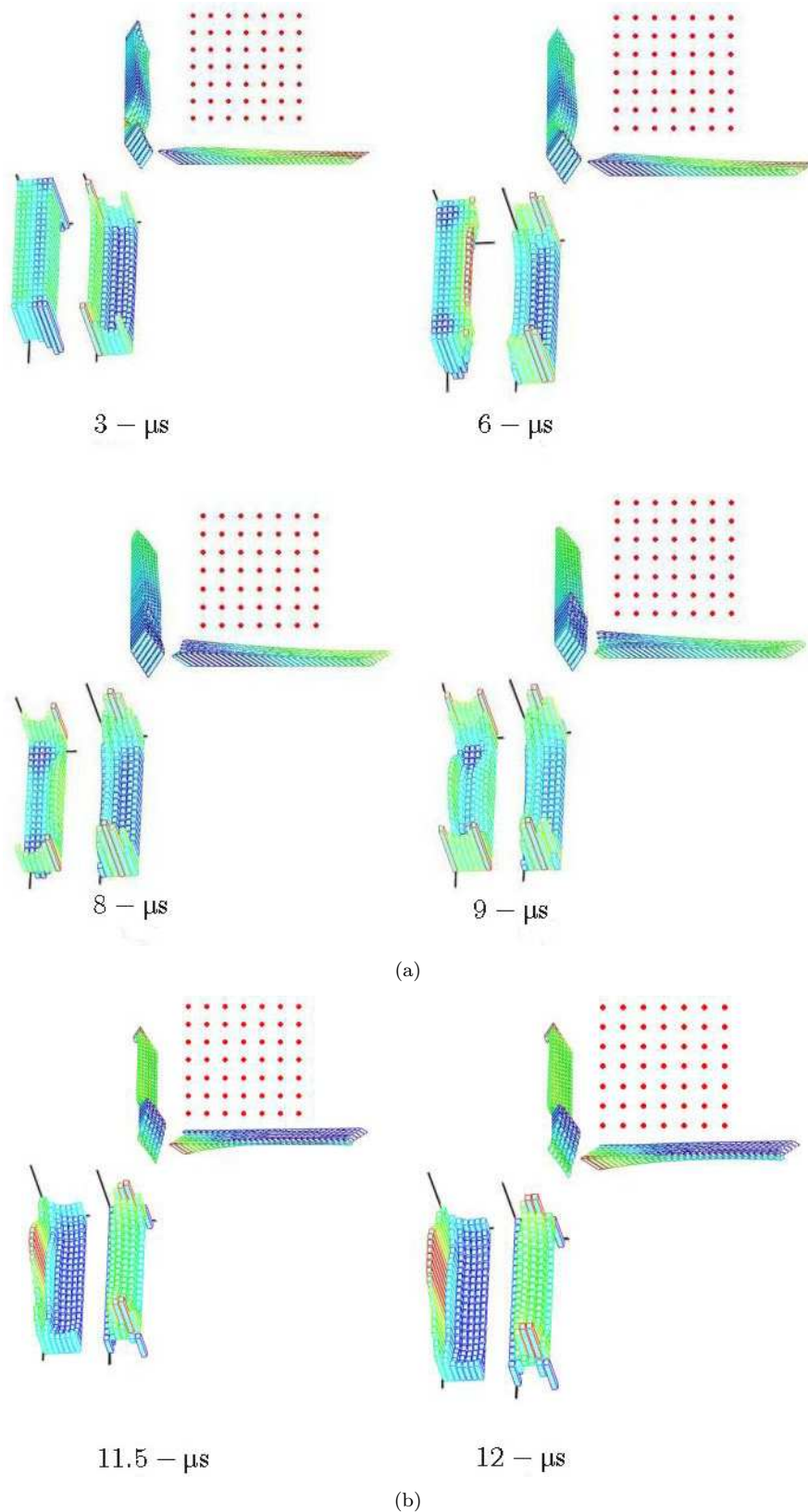


Fig. 14. Current distribution calculated by filamentary modelling for different implosion times during M design liner experiment with initial magnetic field. The filamentary arrangement of the elements as presented in figure 2.

and its time rate-of-change and also the corresponding build up of the initial magnetic field at the liner

centre. The initially high rate-of-change in the current is due to diffusion of the magnetic field through both

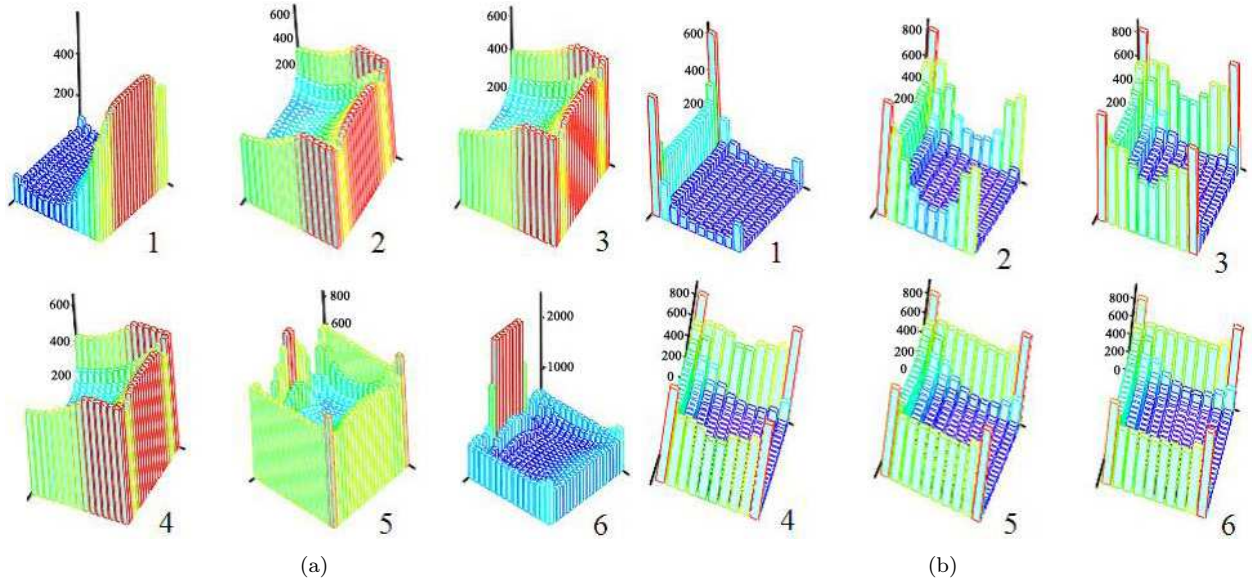


Fig. 15. Temperature distribution (K) a) in liner and b) in driving coil during M design liner experiment with initial field. Corresponding times are: $a = 3 \mu\text{s}$, $b = 6 \mu\text{s}$, $c = 8 \mu\text{s}$, $d = 9 \mu\text{s}$, $e = 11.5 \mu\text{s}$ and $f = 12 \mu\text{s}$. The view is the same as explained in figure 7.

the shields and the liner (the driving coil circuit is open during this time), and the close agreement between theoretical and measured results indicates that magnetic diffusion is accurately described by the model.

Figure 10 shows the predicted distribution of the initial magnetic field within the liner, and indicates clearly that the magnetic field is certainly not uniform. Both this feature and the overall accuracy of prediction were confirmed during preliminary testing, by measurements using 35-turn coils wound on a 4.4 mm plastic mandrel. The evident nonuniformity will certainly affect the liner dynamics, and is one of the main reasons why simple models fail to reproduce accurately the details of the flux-compression process.

The liner dynamics are illustrated by figure 11. As peak field conditions are approached the inner surface of the liner becomes less and less regular, and experimental x-ray data becomes more difficult to compare with theoretical predictions. The relatively smooth outer surface of the liner can however be measured, the cross-sectional area calculated by numerically integrating the liner shadow from a digitised picture, and an equivalent inner radius obtained by considering the liner to have a perfectly cylindrical shape. Differences evident between the theoretical and experimental results are probably due to 3D liner dynamics effects reducing the cross section seen in the x-ray pictures.

Magnetic field histories recorded during flux-compression experiments with and without an injected initial magnetic field by probes of outer diameter 2.45 mm are presented in figures 12 and 13. The peak (central) field achieved is accurately predicted without

field injection, and the 17 % error when the initial field is present is assumed to be caused by 3D liner dynamics.

Further calculations highlighted that, if the implosion is not centred on the axis, a negative modulation appears in the time rate-of-change of the flux density close to the peak field, an effect related to the liner shape. In some cases this modulation can be sufficiently well pronounced for it to produce an oscillation in the field itself in the final moments of the implosion, and this previously un-commented effect may nevertheless be seen in most existing experimental data [17–19].

A complete history of the current distribution in all the elements of the system is presented in figure 14 where, for presentational simplicity, the position and the shape of both liner and driving coil are regarded as stationary. The corresponding history of the currents in the shields is given in figure 15. The relatively low level of the induced currents prevents any significant mechanical and thermal damage. Finally, figure 16 presents the temperature distribution in both the liner and the driving coil during flux compression. The inner layers of the liner are partially melted just as at the moment of the magnetic field turnaround.

5. Conclusions

A very versatile 2D computer code has been developed for use in designing the experiments and in data interpretation. Even with an initially injected magnetic field, the code is able to predict the central peak field produced with an unprecedented accuracy

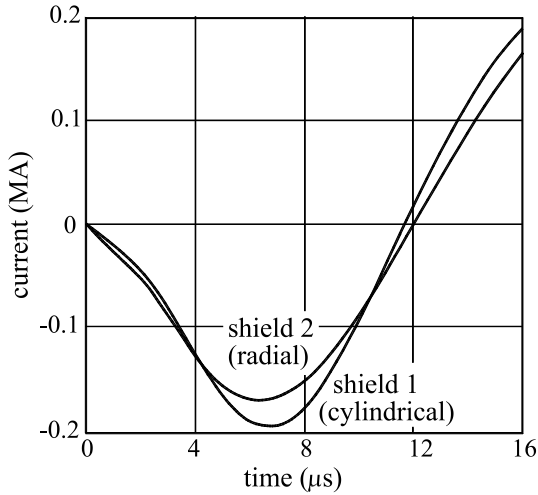


Fig. 16. Total current through the two shields during M design liner experiment with initial field.

of 17 %. With no increase in the available energy, the code confirms that if a (costly) copper liner replaces the present inexpensive aluminium liner the magnetic field produced will be even greater (from 350 T to 430 T).

Many important findings had been made by numerical experimentation; in particular, it was shown that by injecting relatively high initial fields differentially, higher final fields and a higher liner kinetic to capacitor electrostatic energy efficiency can be obtained from a given design with a possible better implosion quality as a bonus.

To obtain even more accurate predictions, a fully 3D code, based on FEA techniques is under development at Loughborough.

Appendix: Electromagnetic force acting on a filament

The total electromagnetic force acting on a body can be calculated from [9]

$$\vec{F} = \oint \vec{T} ds, \quad (A1)$$

where \vec{T} is the vector

$$\vec{T} = \frac{1}{\mu_0} \left[\vec{B} (\vec{B} \cdot \vec{n}) - \frac{1}{2} B^2 \vec{n} \right] \quad (A2)$$

obtained from the multiplication of the column vector \vec{n} with the Maxwell stress tensor, and the integral is evaluated over the entire body surface. It is evident that this force depends only on the magnetic flux density at the surface of the body.

Figure 17 shows a rectangular filament i of infinitely small cross section h_i through which a current I_i is flowing, and with the magnetic flux density at the surface having components \vec{B}_i and \vec{B}_{ext} , produced

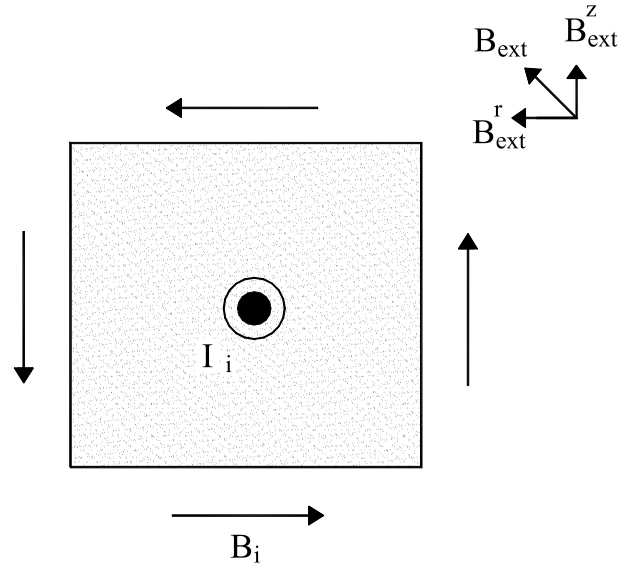


Fig. 17. Circular filament (with rectangular cross section) carrying current I_i and producing surface flux density B_i . External flux density B_{ext} is also shown, together with its radial and axial components.

respectively by its own filamentary current and the sum from all the other filamentary currents. When written in cylindrical components equation (A2) enables the axial and radial components of \vec{T} to be calculated at each surface of the filament, by assuming that the flux density is constant over that surface. Thus, on the upper surface, the axial component is given by

$$T_{upper}^z = \frac{1}{\mu_0} \left[B_{ext}^z B_{ext}^z - \frac{1}{2} (\vec{B}_i - B_{ext}^r)^2 \right]$$

or, on evaluating

$$T_{upper}^z = \frac{1}{\mu_0} \left[(B_{ext}^z)^2 - \frac{1}{2} (B_i - B_{ext}^r)^2 \right]$$

where the superscript on B_i has been omitted since this is constant over all the surfaces.

Similar considerations applied to the other three surfaces show that

$$\begin{aligned} T_{lower}^z &= \frac{1}{\mu_0} \left[-(B_{ext}^z)^2 + \frac{1}{2} (B_i + B_{ext}^r)^2 \right], \\ T_{left}^z &= \frac{1}{\mu_0} \left[B_{ext}^r (B_{ext}^z + B_i) \right], \\ T_{right}^z &= -\frac{1}{\mu_0} \left[B_{ext}^r (B_{ext}^z - B_i) \right] \end{aligned}$$

and, on using equation (A1) with $\oint ds = 2\pi r_i h_i$, it follows that

$$F_i^z = \frac{4}{\mu_0} B_i B_{ext}^r 2\pi r_i h_i. \quad (A3)$$

Applying Ampere's Law $\oint \vec{B}_i d\vec{l} = \mu_0 I_i$ to the filament perimeter leads to $B_i = \frac{\mu_0 I_i}{4h_i}$ and introducing

this result into equation (A3) gives the result for the axial force acting on the filament as

$$F_i^z = I_i B_{ext}^r 2\pi r_i \quad (A4)$$

Similar considerations give a corresponding result for the radial force on the filament as

$$F_i^r = I_i B_{ext}^z 2\pi r_i \quad (A5)$$

a result that is unavailable in most textbooks.

Acknowledgement

The work described was supported by the EPSRC and the MoD through their Joint Grant Scheme (Research Grant GR/R 44645).

Manuscript received January 6, 2005

References

- [1] Novac B.M., Smith I.R., Rankin D.F. and Hubbard M. A fast and compact θ -pinch electromagnetic flux-compression generator // J.Phys.D: Appl.Phys. – 2004. – V. 37 . – P. 3041–3055.
- [2] Latal H.G. Theory of the Cnare effect // Ann.Phys. – 1967. – V. 42. – P. 352–364.
- [3] Freeman J.R., Cnare E.C. and Waag R.C. Magnetically imploded metal foils // Appl. Phys. Lett. – 1967. – V. 10. – P. 111–113.
- [4] Miura N. and Chikazumi S. Computer simulation of megagauss field generation by electromagnetic flux-compression // Jap.J.Appl.Phys. – 1979. – V. 18. – P. 553–564.
- [5] Novac B.M., Smith I.R., Enache M.C. and Senior P. Studies of a very high efficiency electromagnetic launcher // J.Phys.D:Appl.Phys. – 2002. – V. 35. – P. 1447–1457
- [6] Novac B.M. and Smith I.R. Two-dimensional filamentary modelling techniques applied to high-energy pulsed power systems // European Pulsed Power Symposium, Saint-Louis, France, 22–24 Oct. 2002 (IEE: London). – P. 35/1–6.
- [7] Miura N. and Nakao K. Computer analysis of megagauss field generation by condenser bank discharge // Jap.J.Appl.Phys. – 1990. – V. 29 – P. 1580–1599.
- [8] Miura N. and Nojiri H. Recent advances in megagauss physics // Physica B. – 1996. – V. 216. – P. 153–157.
- [9] Smythe W.R. Static and Dynamic Electricity 3rd Edition. – New York: Hemisphere Publ.Corp. – 1989.
- [10] Nakao K., Herlach F., Goto T., Takeyama S., Sakakibara T. and Miura N. A laboratory instrument for generating magnetic fields over 200 T with single turn coils // J.Phys.E: Sci. Instrum. – 1985. – V. 18. – P. 1018–1026.
- [11] Press W.H., Flannery W.T., Teukolsky S.A. and Vetterling B.P. Numerical recipes in C: the art of scientific computing. – New York: Cambridge Univ. Press. – 1992.
- [12] Lyon S.P., Johnson J.D. SESAME: The Los Alamos National Laboratory equation of state data base Report LA-UR-92-3407. – 1992.
- [13] Knoepfel H. Pulsed High Magnetic Fields. – Amsterdam: North Holland Publ. Comp. – 1970.
- [14] Desjarlais M.P. Practical improvements to the Lee-More conductivity near the metal-insulator transition // Contrib Plasma Phys. – 2001. – V. 2–3. – P. 267–270.
also private communication
- [15] Cnare E. Magnetic flux compression by magnetically imploded metallic foils // J.Appl.Phys. – 1966. – V. 37. – P. 3812–3816.
- [16] Novac B.M., Smith I.R., Rankin D.F. and Hubbard M. An insulator-metallic phase transition cascade for improved electromagnetic flux-compression in θ -pinch geometry // IEEE Trans. Plasma Science. – 2004. – V. 32. – P. 1960–1965.
- [17] Miura N., Kido G., Oguro I. and Chikazumi S. Generation of megagauss magnetic fields and their application to solid state physics // Physics in High Magnetic Fields, Colloque internationaux, Grenoble, France (C.N.R.S.: Paris) – 1975. – V. 242. – P. 345–353.
- [18] Miura N., Kido G., Goto T., Miyajima H., Nakao K. and Chkazumi S. Generation of megagauss fields by electromagnetic flux-compression and their use for solid state physics. Ultrahigh Magnetic Fields (Physics.Techniques.Applications) – Moscow: Nauka. ed V.M. Titov and G.A. Shvetsov. – 1984. – P. 117–129.
- [19] Matsuda Y.H., Herlach F., Ikeda S. and Miura N. Generation of 600 T by electromagnetic flux compression with improved implosion symmetry // Rev.Sci.Instr. – 2002. – V. 73. – P. 4288–4294. (Fig. 5, experiments A and B only)